Lighting up dark exomoons: observational signatures of tidally induced volcanism in other worlds

Kleisioti, E.

3 | The spectroastrometric detectability of nearby Solar System-like exomoons

Adapted from

Q. B. van Woerkom, **E. Kleisioti**
Astronomy & Astrophysics, 684, A72 (2024)

Context. Though efforts to detect them have been made with a variety of methods, no technique can claim a successful, confirmed detection of a moon outside the Solar System yet. Moon detection methods are restricted in capability to detecting moons of masses beyond what formation models would suggest, or they require surface temperatures exceeding what tidal heating simulations allow.
Aims. We expand upon spectroastrometry, a method that makes use of the variation of the centre of light with wavelength as the result of an unresolved companion, which has previously been shown to be capable of detecting Earth-analogue moons around nearby exo-Jupiters, with the aim to place bounds on the types of moons detectable using this method.
Methods. We derived a general, analytic expression for the spectroastrometric signal of a moon in any closed Keplerian orbit, as well as a new set of estimates on the noise due to photon noise, pointing inaccuracies, background and instrument noise, and a pixelated detector. This framework was consequently used to derive bounds on the temperature required for Solar System-like moons to be observable around super-Jupiters in nearby systems, with ϵ Indi Ab as an archetype.
Results. We show that such a detection is possible with the ELT for Solar System-like moons of moderate temperatures (150–300 K) in line with existing literature on tidal heating, and that the detection of large (Mars-sized or greater) icy moons of temperatures such as those observed in our Solar System in the very nearest systems may be feasible.

3.1 Introduction

The Solar System hosts a variety of large moons, presenting environments as diverse and scientifically interesting as its planets. As the count of exoplanets found so far is in the thousands, it is natural to ask whether these extrasolar planets hide an equal number of extrasolar moons. Secondary or population-level effects of such moons have already been found (e.g. Kenworthy &Mamajek 2015; Hippke 2015; Teachey et al. 2018; Oza et al. 2019; Saillenfest et al. 2023), and so the question is not whether these moons exist, but rather what they look like, and in what systems and around which planets can they be found.

The detection and characterisation of such satellites accompanying extrasolar planets holds the potential to further our understanding of planet formation, evolution, and habitability. Different moon and planet formation scenarios and their outcomes have been linked to predictions of or requirements on, for example, the time of formation of the satellites (Cilibrasi et al., 2018), their size and mass relative to their host (Nakajima et al., 2022; Canup &Ward, 2006; Hansen, 2019), circumplanetary disc (CPD) composition (Batygin &Morbidelli, 2020; Oberg et al., 2023), host magnetosphere (Canup &Ward, 2006), host mass (Oberg et al., 2023), instellation or host migration history (Heller &Pudritz, 2015a,b), and orbital properties (Li et al., 2020). While the Solar System is host to a large number of moons, the limited scenario we are presented with cannot conclusively bear witness to any of these analyses: validation of these formation studies would require the detection and characterisation of satellites of planets outside the Solar System.

Moreover, moons with the mass of Mars or greater (which are not found in the Solar System) are promising targets for habitability studies (Lammer et al., 2014; Williams et al., 1997; Dobos et al., 2022; Forgan &Dobos, 2016), and the observationally confirmed existence of subsurface oceans on Titan (Beuthe, 2015; Bills &Nimmo, 2011; Baland et al., 2011), Enceladus (Beuthe, 2016), among others, and the likely current or past existence of such oceans on Triton (Nimmo &Spencer, 2015; Schenk et al., 2021; McKinnon &Kirk, 2014; Gaeman et al., 2012) and other Solar System bodies (e.g. Hussmann et al. 2006; Burnett &Hayne 2023; Rovira-Navarro et al. 2023; Nimmo et al. 2016; Bagheri et al. 2022; Bierson &Nimmo 2022; Nimmo &Pappalardo 2016) hold promise for the potential habitability of such worlds, even at sizes observed in the Solar System. This makes Solar System-like satellites objects of interest concerning habitability in their own right, not just as extensions of the population of small icy and rocky planets orbiting stars directly.

Current searches for exomoons are limited primarily to those using transit timing variations (TTVs) and transit duration variations (TDVs), which can yield orbital and mass information on the moon (Kipping, 2009a,b; Heller et al., 2014; Teachey et al., 2018, 2020; Fox &Wiegert, 2021; Kipping &Yahalomi, 2022; Kipping et al., 2022). For this method, unfortunately, the effects of even large moons are degenerate with those produced by other, potentially unobserved planets in the system (Fox &Wiegert, 2021; Kipping &Teachey, 2020). Consequently, candidate moons are met with skepticism (Teachey et al., 2020; Fox &Wiegert, 2021; Kipping, 2020; Tokadjian &Piro, 2022), especially as they have thus far required invoking eccentric formation scenarios (Hamers &Portegies Zwart, 2018; Hansen, 2019; Kipping et al., 2022). Other detection and characterisa-

tion methods have been proposed, from those directly analogous to those used in planet detection such as radial velocity measurements of the host planet (Ruffio et al., 2023; Vanderburg et al., 2018) or transit spectroscopy (Kaltenegger, 2010; Limbach et al., 2021) to the detection of thermal excesses in direct imaging data (Limbach &Turner, 2013; Kleisioti et al., 2021, 2023) or microlensing (Han &Han, 2002; Han, 2008; Hwang et al., 2018). These also face major limitations, however. The first two methods, with current instrumentation, can unfortunately only detect binary-like satellites in terms of size and mass (Lazzoni et al., 2022), whereas the third requires exceptional tidal heating rates. Microlensing detections are isolated events, and therefore are difficult to confirm and cannot be followed up on.

In this analysis, we build upon previous work by Cabrera &Schneider (2007), who discussed the possibility of detecting extrasolar satellites by astrometry of the planet or photometric phenomena induced by mutually eclipsing and dimming events, and Agol et al. (2015), who put these two together and discussed the possibility of detecting extrasolar satellites by use of a method called spectroastrometry, in which one measures the differential on-sky position between the light originating from a system in different filters. A shift in the centre of light between two filters cannot be the result of a point-source or symmetric object (e.g. rings), and so explanation of such a shift in a planet signal requires the presence of a (potentially unresolved) second object. This method has previously found use in characterisation of close-separation stellar binaries and active galactic nuclei at scales well below the diffraction limit, as the centroid can be measured to precision better than the diffraction or seeing limits (Bailey, 1998a,b; Porter et al., 2004; Whelan &Garcia, 2008).

Bailey (1998b) already predicted that '... a large telescope using low-order adaptive optics to achieve image sizes of $\sim$ 0.1 arc second in the IR should be able to use spectroastrometry to make measurements to $\sim$ 100 micro-arcsec', which is roughly equivalent to the separations of Solar System-like moons at distances of the order of tens of parsecs. We derive improved estimates of the signal and noise for spectroastrometry of photometric points, and we show that the upcoming class of extremely large telescopes (ELTs), with the European ELT as archetype, will indeed be capable of detecting and characterising nearby mild-to-warm tidally heated exomoons (THEMs) of sizes and separations such as those found in our Solar System and compatible with moon formation theory, with relatively little regard for inclination or orientation of the satellite orbit.

In contrast, satellites with the expected mass ratios of $\sim 10^{-4}$ compared to their host predicted by Canup &Ward (2006) at medium-to-wide planet-moon separations will remain elusive even with future instrumentation for most other methods (Ruffio et al., 2023; Lazzoni et al., 2022). Additionally, those other methods impose a restrictive orientation of the orbit of the satellite (for planet-transiting moons or radial velocity detections; Lazzoni et al. 2022) or require a fortituous transiting orientation of the host planet with respect to its star (Kipping, 2009a,b). We show that spectroastrometry only imposes a weak orientation preference on observations that is complementary to that required for the radial velocity and planet-transit methods.

We structure the analysis as follows: we begin by presenting the spectroastrometric signal, noise, and some their basic and derived properties in Sections 3.2.1 to 3.2.5, followed by a description of our benchmark scenario in Section 3.2.6. The results for this

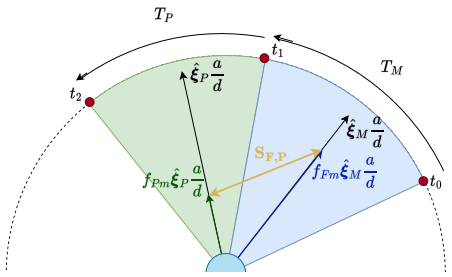

Figure 3.1: Illustration of the geometry underlying the calculation of the spectroastrometric signal in the face-on case ($p = 1$).

benchmark scenario are presented in Section 3.3, and the limitations of our analysis, the repercussions with respect to current-generation telescopes, and a comparison with other moon detection and characterisation methods are presented in Section 3.4. We conclude matters in Section 3.5.

3.2 Methods

In the following, we present the framework upon which our analysis is based. It is structured as follows: in Sections 3.2.1 and 3.2.2 we introduce the spectroastrometric signal and some of its basic properties, followed by a discussion on the contaminating noise sources in Section 3.2.3 and the consequences on observation design in Section 3.2.4. We then derive an expression for the minimum flux a moon must have to be detectable at a given signal-to-noise ratio given any instrument specifications in Section 3.2.5, and introduce the model scenario used to evaluate the efficacy of spectroastrometry in detecting Solar System-like moons in Section 3.2.6.

3.2.1 The centroid and the spectroastrometric signal

In defining the spectroastrometric signal, we take an approach that differs from that taken by Agol et al. (2015); this framework allows us to compute several additional error estimates. Motivated by the idealised mathematical limit of the photon-count averaged centre of light on a detector D for ever smaller pixels, we shall define the centroid for an observation over a time interval T_F through a filter F, $\mathbf{c}_F$, as the photon count-weighted integral over all positions $\mathbf{c}$ over the course of an observation O, during which a total of N_F photons are counted as follows:

$$\mathbf{c}_F = \frac{1}{N_F} \int_{O,D} \mathbf{c} N_F(\mathbf{c}). \tag{3.1}$$

The differential photon count hitting the detector for each position $\mathbf{c}$, $N_F(\mathbf{c})$, can be rewritten, accounting for the fact that the incoming photon rate is a function of the detector location it hits and of time, t. We choose to ignore the effect of the photon path through the instrument, such that we can then write $N_F(\mathbf{c}) = I_F(\mathbf{c}, t)\Omega t S$ with I_F the photon intensity through the filter F originating from the point $\mathbf{c}$ on the celestial sphere at time t, Ω the

infinitesimal area on the detector that the photons hit (expressed as solid angle on the celestial sphere), and S the infinitesimal area of the telescope aperture that the photon field passes through. If we furthermore assume that the total photon flux originating from the part of the sky we observe through the filter F, $F_F = \int_D I_F(\mathbf{c}, t)\Omega$, is constant throughout the observation such that $N_F = F_F T_F S$, we obtain:

$$\mathbf{c}_F = \frac{1}{T}\int_T \left(\frac{1}{F_F}\int_D \mathbf{c} I_F(\mathbf{c}, t)\Omega\right) t \tag{3.2}$$

where S was taken outside the integral as we had assumed the photon flux on the detector to be independent of the photon path through the instrument. The outermost integral is ostensibly a time-average, while

$$\mathbf{c}_F(t) = \frac{1}{F_F}\int_D \mathbf{c} I_F(\mathbf{c}, t)\Omega \tag{3.3}$$

is the photon flux-averaged centre of light at time t. We have thus shown that the centroid as measured from an observation is the time-averaged value of the instantaneous centroid $\mathbf{c}_F(t)$ over the duration of that observation: $\mathbf{c}_F = \langle \mathbf{c}_F(t)\rangle_T$.

We note that for an $I_F(\mathbf{c}, t)$ that is point-symmetric about some point $\mathbf{c}_0(t)$ we have $\mathbf{c}_F(t) = \mathbf{c}_0(t)$: motivated by this observation, we shall now assume that we are observing a planet-moon system (we note, however, that computation of the centroid of an observation according to Eq. 3.1 does not require this assumption), such that we can decompose the intensity originating from any given on-sky location into that originating from the planet (denoted by the subscript p) and that originating from the moon (with the corresponding subscript m). Then, by linearity of the integral:

$$\mathbf{c}_F = \frac{F_{Fp}}{F_F}\left\langle \mathbf{c}_{Fp}(t)\right\rangle_{T_F} + \frac{F_{Fm}}{F_F}\left\langle \mathbf{c}_{Fm}(t)\right\rangle_{T_F} \tag{3.4}$$

where F_{Fp} (respectively F_{Fm}) is the flux in the filter F due to the planet (respectively moon). We observe that so long as the point-spread function (PSF) for our telescope is point-symmetric, we have that the components $I_{Fp}(\mathbf{c}, t)$ and $I_{Fm}(\mathbf{c}, t)$ of our intensity are respectively point-symmetric about the on-sky position of the planet and moon, which we shall denote $\mathbf{c}_p$ and $\mathbf{c}_m$, such that finally:

$$\mathbf{c}_F = \left\langle \mathbf{c}_p(t)\right\rangle_{T_F} + \frac{F_{Fm}}{F_F}\left\langle \mathbf{c}_m(t) - \mathbf{c}_p(t)\right\rangle_{T_F}, \tag{3.5}$$

analogous to Eq. 4 in Agol et al. (2015). We must note, though, that here we have shown that filter fluxes must be expressed in photon fluxes, not energy fluxes, for this relation to hold. For notational brevity, we shall henceforth write $\mathbf{c}_m(t) - \mathbf{c}_p(t) = \mathbf{c}_{mp}(t)$ for the on-sky projected angular separation of the two bodies. In imitation of the approach Agol et al. (2015) take to forego the necessity of a reference position, we then define the spectroastrometric signal $S_{M,P}$ as the absolute difference between the centroid location in a filter M in which we expect to observe the moon (the 'moon filter'; not to be confused with the notation for absolute magnitude used in other literature) and another filter P in which we

expect the planet to be dominant (the 'planet filter'); we remark that we also differentiate between the periods over which the two observations were made, T_M and T_P respectively:

$$\begin{aligned} S_{M,P} &= |\mathbf{c}_M - \mathbf{c}_P| \\ &= \left| \frac{F_{Mm}}{F_M} \left\langle \mathbf{c}_{mp}(t) \right\rangle_{T_M} - \frac{F_{Pm}}{F_P} \left\langle \mathbf{c}_{mp}(t) \right\rangle_{T_P} \right| \end{aligned} \tag{3.6}$$

where we have assumed that the time-averaged position of the planet over both the periods T_M and T_P is identical. As we shall encounter these quantities more often, let us denote the fraction of the flux in the band M (respectively P) due to the moon, $\frac{F_{Mm}}{F_M}$ (respectively $\frac{F_{Pm}}{F_P}$), as f_{Mm} (respectively f_{Pm}).

3.2.2 The spectroastrometric signal for closed Keplerian orbits

For $\left\langle \mathbf{c}_{mp}(t) \right\rangle$ an analytic solution exists in terms of known quantities from orbital mechanics for all closed Keplerian orbits. One can then show that the expected value of the signal for a given observation of a moon with unconstrained inclination i and ω (i.e. a flat prior on both i and ω) is given by:

$$S_{M,P} = \frac{\gamma a f_{Mm}}{d} \left| \hat{\boldsymbol{\xi}}_F - \frac{f_{Pm}}{f_{Mm}} \hat{\boldsymbol{\xi}}_P \right| \tag{3.7}$$

with γ a parameter describing our knowledge of the inclination i and orientation (through ω) of the moon; if i and ω are unconstrained (i.e. uniformly distributed), we have $p \approx 0.842$ if instead the moon is positioned in the worst possible orientation (edge-on i.e. $i = \pi/2$), we have $p = 2/\pi$; in the best possible orientation (face-on i.e. $i = 0$) we have $p = 1$. $\hat{\boldsymbol{\xi}}_M$ (respectively $\hat{\boldsymbol{\xi}}_P$) is the non-dimensionalised time-averaged in-orbit position over the time period T_M (respectively T_P) of the moon, and d is the system-observer distance. An illustration of the geometry involved is given in Fig. 3.1.

It will suffice for now to know that it can be shown that the time-averaged in-orbit position depends on the orbital properties of the moon according to Eq. 3.8:

$$\hat{\boldsymbol{\xi}} = \frac{P}{2\pi T} \begin{pmatrix} (1 - \frac{e^2}{2}) \sin E - \frac{e}{4} \sin 2E \\ (1 - e^2)^{1/2} \left(\frac{e}{4} \cos 2E - \cos E \right) \end{pmatrix} \Bigg|_{E_0}^{E_1} - \begin{pmatrix} \frac{3e}{2} \\ 0 \end{pmatrix} \tag{3.8}$$

where P (not to be confused with the filter P, which only appears in subscripts) and e are the period and eccentricity of the orbit of the moon, T is the timespan over which we observe in the filter of interest, and E_0 and E_1 are the eccentric anomaly at the start and end of the observation in that same filter, respectively. For a given time since periapsis, E_0 and E_1 can be calculated by solving Kepler's equation, for which a variety of solution methods exist; we employ the non-iterative method described by Markley (1995).

3.2.3 Sources of spectroastrometric noise

There are, however, several sources of noise that will contaminate the signal. In the following, we shall describe relevant noise sources and their corresponding expressions,

as follows: (1) photon shot noise, (2) pixel noise, (3) background and instrument flux noise and (4) pointing noise. We (will) note that each of these noise sources acts upon each of the measured centroids individually (that is, per filter) and independently. We will therefore consider in the following the noise that each of these sources imparts upon the measured centroid in a filter, noting that these noise sources are present in both the filter M and the filter P. We can then combine the two into the resulting total noise for the spectroastrometric signal in Sec. 3.2.3.

Photon noise

The PSF of the telescope is not just the reason by which we cannot resolve the moon and planet directly on the exposure; the resulting spread in photon arrival locations causes an inherent and unavoidable variance in the measured centroid, given that we can only ever take a finite sample of the PSF. Under the condition of point symmetry of the PSF we have for the photon noise σ_{PN}:

$$\sigma_{PN} = \frac{\sigma_{PSF}}{\sqrt{N}} \tag{3.9}$$

where σ_{PSF} is the standard deviation of the PSF for a single sample (i.e. a single photon) and N is the number of photons observed in the filter. For a diffraction-limited telescope, the Gaussian approximation of the Airy disc used by Agol et al. (2015), where $\sigma_{PSF} = 0.45\lambda_c/D$ (with λ_c the central wavelength of the observation filter and D the telescope diameter), gives a useful general expression, but where available an estimate from PSF shape models would of course be preferred. As we use the ELT as archetype for the full class of extremely large telescopes (for which PSF models are not yet available), we will use the expression by Agol et al. (2015) in our simulations, but prefer to retain σ_{PSF} in expressions.

Pixel noise

Another source of noise derives from the fact that we are not probing the actual on-sky intensity distribution, but a pixelated version thereof. The finite size of the pixels on our detectors means that we lose some information about each detected photon. An upper bound for the noise that this introduces is given by

$$\sigma_{px} = \frac{\alpha}{\sqrt{2N}} \tag{3.10}$$

with α the pixel width, and N again the total number of photons observed in the filter.

Background and instrument flux noise

The noise in background and instrument flux will also give rise to noise in the measured centroid. An upper bound for this contribution is given by

$$\sigma_n = \sqrt{\frac{6}{5}}\left(\frac{1}{6}\left\lceil\frac{6\sigma_{PSF}}{\alpha}\right\rceil\right)\frac{\alpha}{\sqrt{N}} \tag{3.11}$$

under the assumptions that the planet detection in the flux is $\geq 5\sigma$, that we sample the centroid from the detector region encompassing the 3σ-region of the PSF (which contains $> 97\%$ of the incoming flux) and that the noise is uncorrelated between pixels.

Pointing noise

The imperfect pointing accuracy of the telescope will also impact the extracted centroid; we can account for this by assuming that each observed photon has a further random offset dictated by the pointing accuracy of the telescope. In that case, the mathematical framework works out precisely as for the PSF, so long as the timescale on which the telescope pointing is affected by inaccuracies is significantly lower than the total time of the exposure, such that photons can be assumed to be independently affected. In the case of the ELT, the uncompensatable random errors vary on subsecond timescales (Rodeghiero et al., 2021), such that we deem this a reasonable assumption. METIS will achieve fine-guiding accuracies below $0.02\lambda/D$ (Brandl et al., 2021), which translates to a worst-case pointing offset below $\sigma_{PO} \approx 1$ mas, such that we can expect the pointing inaccuracy σ_p to be at the very greatest

$$\sigma_p = \frac{\sigma_{PO}}{\sqrt{N}}. \tag{3.12}$$

This term is negligible for the ELT, but may be important or even limiting for space telescopes in particular.

This treatment then accounts for random pointing noise; systematic pointing offsets can be removed by referencing against the reference objects used. If possible with the given coronagraphic system, the central star or another bright co-moving object would be a suitable candidate. Otherwise, a background object can be used. As such objects are in general far brighter than the planet, the corresponding spectroastrometric noise is likely to be negligible. If the telescope reacquisition pointing accuracy between different filters allows for it, referencing against other objects may even become unnecessary. This may introduce systematic bias if there is an unknown offset between filters (e.g. due to imperfect adaptive optics), however, and so this should be carefully accounted for.

Total noise

The fact that all noise sources go as $N^{-1/2}$ motivates us to combine them into one term, such that we can describe the total noise in a filter as $\sigma_{tot} = \sigma N^{-1/2}$. We can consider the noise σ to be an 'effective noise per photon', and under the assumption that all noise sources are independent we can calculate σ to be

$$\begin{aligned}\sigma &= \sqrt{N}\sigma_{tot} = \sqrt{\sigma_{PN}^2 + \sigma_{px}^2 + \sigma_n^2 + \sigma_p^2} \\ &= \sqrt{\sigma_{PSF}^2 + \sigma_{PO}^2 + \left(\frac{1}{2} + \frac{1}{30}\left\lceil\frac{6\sigma_{PSF}}{\alpha}\right\rceil^2\right)\alpha^2}.\end{aligned} \tag{3.13}$$

It is instructive to remark that σ for the both filters, σ_M and σ_P, is a property inherent to a given filter on a given telescope, but it does not depend on the object to be observed.

The combined noise σ affects the measured centroids of both of the filters in question. Assuming that these two measured centroids are statistically independent, the total noise in the measured spectroastrometric signal, σ_S, is then:

$$\begin{aligned}\sigma_S &= \sqrt{\sigma_{tot,M}^2 + \sigma_{tot,P}^2} = \sqrt{\frac{\sigma_M^2}{N_M} + \frac{\sigma_P^2}{N_P}} \\ &= \frac{1}{\sqrt{S_{eff}\varepsilon}} \sqrt{\frac{\sigma_M^2(1-f_{Mm})}{F_{Mp}T_M} + \frac{\sigma_P^2(1-f_{Pm})}{F_{Pp}T_P}}\end{aligned} \tag{3.14}$$

with ε being the achromatic efficiency of the telescope and S_{eff} its effective surface area, where we have used that $N_M = S_{eff}\varepsilon T_M F_{Mp}/(1-f_{Mm})$ (an analogous expression of course holds for N_P).

Note that it follows directly from Eq. 3.14 that the best planet filter P to observe in so as to minimise the noise is the one in which F_{Pp}/σ_P^2 is maximised; the same conclusion holds for the moon filter F, so long as the moon is expected to be sufficiently luminous in this filter, too.

3.2.4 Consequences for the observation time allocation

From Sec. 3.2.3 we can conclude an important guideline for observations: namely, one can show that given a fixed total observation time $T = T_M + T_P$, there exists an allocation between T_M and T_P such that σ_S as given by Eq. 3.14 is optimised. This time allocation can be shown to satisfy the relation

$$\frac{T_M}{T_P} = \frac{\sigma_M}{\sigma_P}\sqrt{\frac{F_{Pp}}{F_{Mp}}}\sqrt{\frac{1-f_{Mm}}{1-f_{Pm}}} \approx \frac{\sigma_M}{\sigma_P}\sqrt{\frac{F_{Pp}}{F_{Mp}}}. \tag{3.15}$$

The approximation is justified by noting that for a suitable planet filter P we ought to expect that $f_{Pm} \approx 0$, and if the moon does not fully dominate in M, $\sqrt{1-f_{Mm}} \approx 1$ is also reasonable. As this approximated optimal time allocation requires no a priori knowledge of any tentative moon, we find it most representative to perform our evaluation of the method using this time allocation. We wish to note that this optimal time allocation is equally valid for the noise estimate used by Agol et al. (2015), though they do not appear to have taken note of it.

3.2.5 Minimum required moon flux

In general, unfortunately, we have no a priori knowledge of the expected flux of moons. Moreover, we are interested not in the signal-to-noise ratio produced by a specific moon, but rather we would like to answer the converse question: the luminosity a moon ought to have such that it is detectable with at least a given signal-to-noise ratio S/N. One can take Eqs. 3.7 and 3.14 to arrive, after some manipulation, at a criterion for detectability:

$$\begin{aligned}\hat{\boldsymbol{\xi}}_M^2 f_{Mm}^2 + \left(C_M - 2f_{Pm}\hat{\boldsymbol{\xi}}_M \cdot \hat{\boldsymbol{\xi}}_P\right) f_{Mm} \geq \\ C_M + C_P - f_{Pm}^2 \hat{\boldsymbol{\xi}}_P^2,\end{aligned} \tag{3.16}$$

where

$$C_M = \left(\frac{S/Nd\sigma_M}{a\gamma}\right)^2 \frac{1}{\varepsilon S_{eff} F_{Mp} T_M}, \tag{3.17}$$

$$C_P = \left(\frac{S/Nd\sigma_P}{a\gamma}\right)^2 \frac{1 - f_{Pm}}{\varepsilon S_{eff} F_{Pp} T_P}. \tag{3.18}$$

This is a quadratic form in f_{Fm}, whence one can derive the following minimum flux requirement for detectability at the specified signal-to-noise ratio:

$$\frac{F_{Mm}}{F_{Mp}} \geq \frac{A + \sqrt{B}}{D} \tag{3.19}$$

with

$$A = \frac{C_M}{2} + C_P + f_{Pm}\hat{\boldsymbol{\xi}}_M \cdot \hat{\boldsymbol{\xi}}_P - f_{Pm}^2 \hat{\boldsymbol{\xi}}_P^2 \tag{3.20}$$

$$B = \left(\frac{C_M}{2} - f_{Pm}\hat{\boldsymbol{\xi}}_M \cdot \hat{\boldsymbol{\xi}}_P\right)^2 - \hat{\boldsymbol{\xi}}_M^2 \left(f_{Pm}^2 \hat{\boldsymbol{\xi}}_P^2 - C_M - C_P\right) \tag{3.21}$$

$$D = \left(\hat{\boldsymbol{\xi}}_M - f_{Pm}\hat{\boldsymbol{\xi}}_P\right)^2 - C_P. \tag{3.22}$$

This, should be stressed, holds for all closed Keplerian orbits, given the expression for $\hat{\boldsymbol{\xi}}$ in the form of Eq. 3.8, so long as $D > 0$. This latter constraint follows when writing Eq. 3.16 as a form that is quadratic in F_{Mm}/F_{Mp}, and it is satisfied roughly when $C_P \lesssim 1$ such that

$$\frac{S/N\sigma_P}{\sqrt{\epsilon S_{eff} F_{Pp} T_P}} \lesssim \frac{a\gamma}{d}. \tag{3.23}$$

Note that the moon fluxes in either band are, of course, both unknown quantities; as f_{Pm} is relatively low (close to zero) if a suitable planet filter P was chosen, it is more informative (and receptive to implicit computation) to put constraints on F_{Mm} as a function of f_{Pm} than the other way around. If one can relate f_{Mm} and f_{Pm} to a set of defining parameters (say, for example, the surface temperature and radius of a moon), it is then possible to solve the constraint posed by Eq. 3.19 implicitly, given a set of orbital and observation parameters.

3.2.6 Model scenario

To assess the limits of what types of Solar System-like moons may be detectable in nearby systems in the near-future using ELT-class telescopes, we explore a benchmark scenario. We take METIS as reference instrument, given that its capability to detect Earth-sized planets around nearby stars in thermal emission has been well-established (Brandl et al., 2021); it should therefore not be problematic to reach a 5σ detection (in flux) of a giant planet, so as to satisfy the assumptions required for Eq. 3.11. The telescope model parameters are summarised in Table 3.1. For the moon filter M, we take the $N2$-filter as it is the longest-wavelength continuum filter on METIS, which will therefore be best-suited

Table 3.1: Telescope and system model parameters used in the benchmark scenario.

Quantity	Value	Reference
METIS/ELT properties		
Planet filter P	M'	-
Moon filter M	$N2$	-
Diameter [m]	37	C20
System throughput [-]	0.36	C20
Atmospheric transmission [-]	0.8	J13, N12
σ_{PSF} in P [mas]	12.0	-
σ_{PSF} in M [mas]	28.1	-
Model system properties		
Reference distance [pc]	3.6481	P16, V23
Planet mass [M_{Jup}]	3.25	F19
Age [Gyr]	> 3.0	F19

C20: Carlomagno et al. (2020); J13: Jones et al. (2013); N12: Noll et al. (2012); P16: Prusti et al. (2016); V23: Vallenari et al. (2023); F19: Feng et al. (2019). Brandl et al. (2021) give an overview of the METIS optical system and pixel sizes.

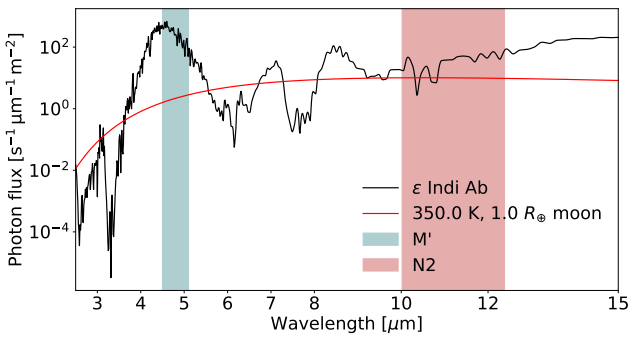

Figure 3.2: Spectrum for ε Indi Ab, generated from *ATMO2020* assuming a 3.25 M_{Jup}, 3 Gyr planet, and equilibrium chemistry; the chosen M' and $N2$ bands are marked. Also shown is the extreme scenario of a 350 K, Earth-sized blackbody moon, for which it is clear that the planet still dominates by $\sim$ 2 orders of magnitude in M', while the moon contributes an appreciable fraction of the flux in $N2$, such that a spectroastrometric signal may be observed between the two filters. We note that the region from 5.5-7.5 μm, though it has promising absorption regions, is inaccessible from the ground.

to capture low-temperature (< 300 K) thermal emission. For the planet filter P, by contrast, we choose the near-infrared filter M', which captures a region in which giant planets such as Jupiter, Saturn (Roman, 2023) and higher-mass exoplanets (Phillips et al., 2020) are luminous, while remaining stiff to the types of temperatures expected globally for tidally heated moons (see e.g. Dobos &Turner 2015). As an example, the used spectrum for ε Indi Ab (which we shall justify shortly) is shown with a 350 K, Earth-sized moon (representing an upper bound on the hottest, largest plausible moons) for comparison in Fig 3.2: it is clear that the planet still dominates wholly in M', while the moon has an appreciable contribution in $N2$. METIS requirements mandate that its optical system is diffraction-limited (Brandl et al., 2021), which we will therefore take as an assumption on the PSF-width. Atmospheric transmission is set to an achromatic 80%, based on a representative scenario simulated using ESO's *SkyCalc* (Jones et al., 2013; Noll et al., 2012). We set an observation time of 6 hours, representing a length of night that can be reasonably expected to occur regularly at the ELT site (Lombardi et al., 2009), though we note that with a scaling of the noise with $T^{-1/2}$, our results are relatively stiff to the total observation time.

We model a reference moon-planet system based on ε Indi Ab, the nearest Jupiter analogue known imageable by JWST (and thus, presumably, ELT), and its nominal parameters as determined by Feng et al. (2019). The parameters necessary for this analysis are given in Table 3.1; based on this planet mass and age, a spectrum is interpolated from the chemical equilibrium atmosphere-spectra in the publically available atmosphere library *ATMO2020* by Phillips et al. (2020). As their simulated atmospheres only provide data for planets of this mass up to ages of $\sim$ 3 Gyr, we cannot take an age in the age range of 3.7 – 4.3 provided by Feng et al. (2019), though we note that preliminary results using *ATMO2020* show that in this case the spectroastrometric signal-to-noise ratio is increasing with age of the planet (i.e. with decreasing temperature): this makes an age of 3 Gyr conservative.

In imitation of Solar System moons (with the notable exception of Titan), we assume the moon to be an airless icy or rocky body. In such a case, the observed brightness temperature in the infrared agree relatively well with the surface temperature (to within a couple $\sim$ 10 K), regardless of surface material (see e.g. Hu et al. 2012; Whittaker et al. 2022); integrated brightness temperatures of Jupiter's icy moons Ganymede and Callisto agree relatively well with their expected surface temperatures (Squyres, 1980). We therefore choose to model the moon as a black body, such that the only free parameters that remain to explore are (1) its size (but notably not directly its mass), (2) its surface temperature and (3) its orbital properties. Each of these we vary over ranges made plausible by a combination of observed Solar System moons and moon formation theory, so as to explore the signal-to-noise ratio of the spectroastrometric signal. In particular, we vary the size between an Io-radius and an Earth-radius, which, allowing the satellite to be either icy or rocky, covers the full range of expected moon masses of 10^{-5} – 10^{-3} host masses for large satellites proposed in literature (e.g. Canup &Ward 2006; Cilibrasi et al. 2018; Moraes et al. 2018). We vary the semi-major axis over the range seen for the Galilean satellites.

While analysis of time-series observations of the system under the assumption of a moon on a Keplerian orbit may allow one to produce higher-significance detections (see

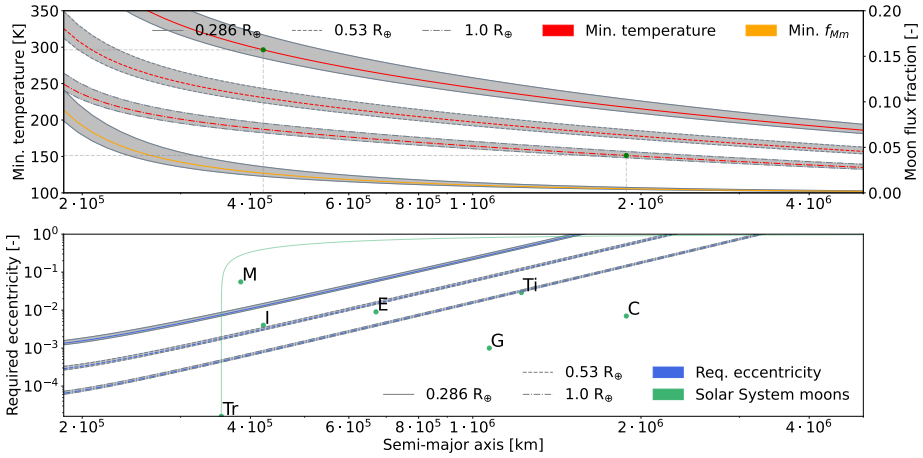

Figure 3.3: Minimum blackbody temperature and corresponding moon flux fraction in M for a total observation time of 6 hours on ELT/METIS as a function of semi-major axis for 5σ detectability of a moon around ε Indi Ab for an Io-sized, Mars-sized, and Earth-sized moon (top), with a corresponding first-order estimate of the required eccentricity (bottom). The grey region delineates the area bounded by the edge-on and face-on cases ($p = 2/\pi$ and $p = 1$); the red and blue lines correspond to the inclination-averaged case ($p \approx 0.842$). Semi-major axes and eccentricities of the seven largest Solar System moons Ganymede, Titan, Callisto, Io, the Moon, Europa and Triton are marked by their first letter(s). The post-capture migration path of Triton assuming conservation of angular momentum (such as in Ross &Schubert 1990) is also marked to illustrate the observational potential of captured moons. The moons used for further analysis in Secs. 3.3.2 and 3.3.3 are marked in green in the top plot. For all three moons over all explored semi-major axes, the minimum 5σ-detectable temperature corresponds to a spectroastrometric signal of roughly 0.013 mas.

Sec. 4.2.2 in Agol et al. (2015) for an example), we prefer to analyse solely the spectroastrometric signal in one observation, as it requires no assumptions on the nature of the signal. A high-significance detection of a spectroastrometric signal would therefore provide incontrovertible evidence of a signal of astrophysical origin, regardless of whether it is a moon or not; further analysis and conclusions on the nature of this signal can then follow.

3.3 Results

We structure our results as follows; we examine the minimum temperature required for detectability in circular orbits as a function of semi-major axis in Sec. 3.3.1, and perform a first-order analysis of the required eccentricities for these temperatures under the assumption that the detectability is only marginally affected by low eccentricities. We

validate this assumption in Sec. 3.3.2, and finally perform an analysis of the attainable signal-to-noise ratios as a function of moon blackbody temperature and distance for two sample moons of given size and semi-major axis in Sec. 3.3.3.

3.3.1 Minimum moon temperature for detectability

Fig. 3.3 shows the minimum required blackbody temperature of a moon for various sizes (corresponding to Io, Mars and the Earth) to be detectable at 5σ in a circular orbit around ε Indi Ab, assuming a total of 6 hours of observation time. Also shown is a first-order estimate of the eccentricities required for each of the various size bodies at each semi-major axis to reach the given minimum temperature by assuming radiative equilibrium of a blackbody moon experiencing viscoelastic dissipation as given by Segatz et al. (1988) and using the value of -Im(k_2) given for Io by Lainey (2016). For comparison, the semi-major axes and eccentricities of the seven largest Solar System moons are marked; as Triton currently has a circular orbit but is known to have migrated to its current position after capture over a timespan of $\sim$ 1 Gyr (Ross &Schubert, 1990; McKinnon &Kirk, 2014), its constant-angular momentum post-capture evolution as described by Ross &Schubert (1990) is also drawn. The value of f_{Mm} corresponding to these minimum temperatures is also shown; over the explored semi-major axis values, f_{Pm} for the minimum detectable temperatures is negligible, and so the required values of f_{Mm} coincide. For this same reason, the spectroastrometric noise is nearly constant across all semi-major axes at $\sim$ 0.0026 mas, corresponding to a minimum detectable spectroastrometric signal of $\sim$ 0.013 mas.

3.3.2 Eccentricity effects

Fig. 3.4 shows the minimum moon blackbody temperature for two sample moons (that will be explored and justified in further detail in Sec. 3.3.3) at an ε Indi Ab-like system-observer distance at a variety of eccentricities and orbital phases covering all possibilities for the inclination-averaged case ($p \approx 0.842$). The green and blue lines, indicating the minimum required temperature for $e = 0$ and ± 10 K deviations from that contour, show that the required temperature for moons with Solar System-like eccentricities ($e \lesssim 0.1$) is in general well-approximated by the required temperature for the circular case throughout the orbit; additionally, the required temperature for detectability is in fact in all cases lower than for the circular case over $> 50\%$ of the orbit.

3.3.3 Applicability to distant systems

The results presented in Secs. 3.3.1 and 3.3.2 suggest that there is a set of nearby systems in which planet-like moons of directly imageable giant planets can be detected. This motivates us to explore the extent of this viable detection space for two scenarios, representing the end-points of what Lazzoni et al. (2022) deem the class of planet-like satellites (namely those formed by core accretion in the CPD, analogous to most Solar System satellites): (1) an Io-sized moon at Io-like separation from its host and (2) an Earth-sized moon at a Callisto-like separation from its host. The first requires the least number of assumptions, as it is a type of moon observed in the Solar System, and tidal

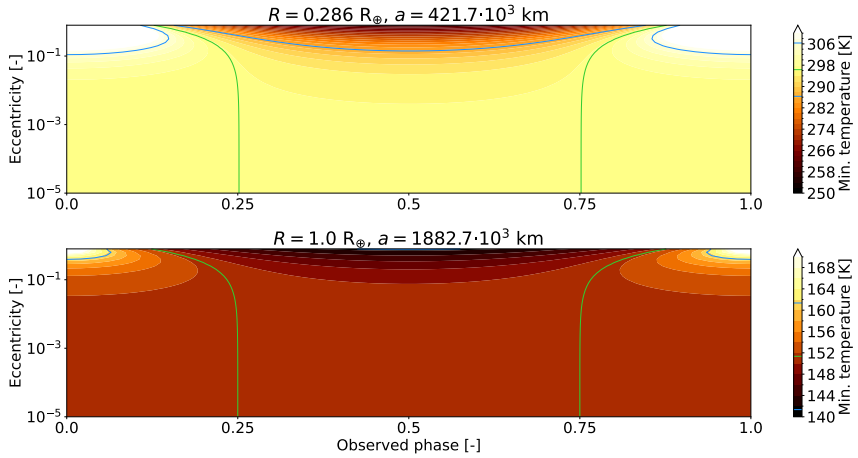

Figure 3.4: Minimum temperature for 5σ detectability as a function of the observed orbital phase and eccentricity for an Io-like moon with an Io-like semi-major axis (top) and for an Earth-like moon with a Callisto-like semi-major axis (bottom). The green and blue contours indicate the contour corresponding to the nominal (zero-eccentricity) required temperature (as marked on the top plot in Fig. 3.3), and the 10 K deviations from this temperature, respectively; in both cases, these are also marked on the colourbar. We note that in all non-zero eccentricity cases the temperature required for observability is in fact lower than for the circular case over > 50% of the orbit.

heating-mechanisms through which it might reach temperatures to be luminous in the IR over observable timescales are well-established (e.g. Dobos &Turner 2015; Rovira-Navarro et al. 2021). The second would be on the larger end of what one expects to see around a host like ε Indi Ab according to moon formation studies such as Canup &Ward (2006), though more recently Cilibrasi et al. (2018) produced results that seem to suggest such masses may be attainable. Additionally, where fixed-Q tidal theory would predict that such a far-out moon should be unlikely to experience significant tidal interactions, the recently proposed paradigm of resonance locking would allow such far-out moons to experience tidal interactions still (Fuller et al., 2016; Lainey et al., 2020). These two cases should therefore in principle bracket the full range of plausible planet-like moons that might be expected to be luminous in the IR; the signal-to-noise ratio as a function of blackbody temperature and system-observer distance for these two cases are illustrated in Fig. 3.5.

3.4 Discussion

Figs. 3.3 and 3.5 indicate that spectroastrometry may be able to provide detections of large icy moons (with surface temperatures as low as $T_s \lesssim 150$ K) or even smaller, hot rocky moons (with surface temperatures as low as $T_s \lesssim 300$ K) in nearby systems; such

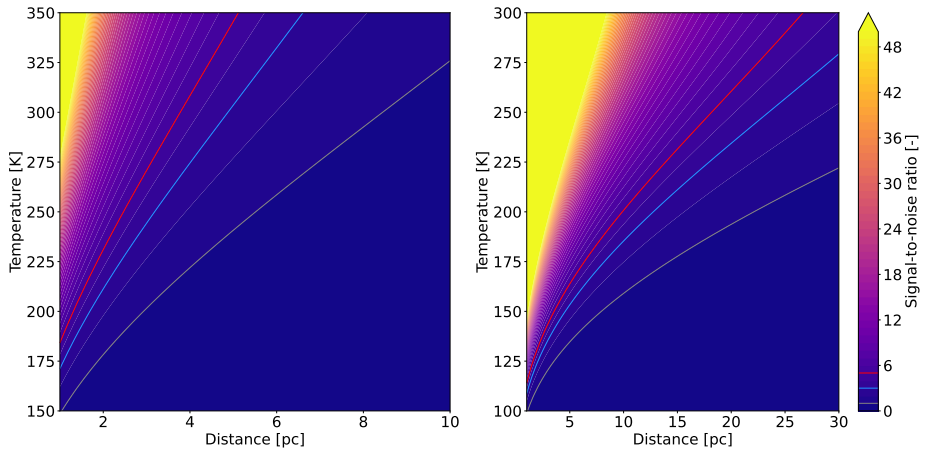

Figure 3.5: Signal-to-noise ratio for an Io-sized moon on an Io-like orbit (left) and an Earth-sized moon on a Callisto-like orbit (right) around an ε Indi Ab-like planet as a function of blackbody temperature and system-observer distance (we note that the axis scale and datum differ between the two moons). The grey, blue, and red lines mark the 1σ, 3σ, and 5σ boundaries, respectively.

temperatures are plausible for tidally heated moons on orbits comparable to modern-day Solar System moons (e.g. Dobos &Turner 2015; Forgan &Dobos 2016; Rovira-Navarro et al. 2021) and easily exceeded by conditions as have been presumed to exist in the early Solar System (e.g. Ross &Schubert 1990), potentially over Gyr timescales (McKinnon &Benner, 1990; Lunine &Nolan, 1992). The possibility of observing large icy moons at low temperatures is interesting, as the large icy moons Ganymede and Callisto in our Solar System have (and are stable at) surface (and brightness) temperatures of order $\sim$ 150 K (Squyres, 1980) (though a large part of this is contributed by solar flux), and the largest and most massive moons are thought to form at or beyond the ice line of their CPD (Heller &Pudritz, 2015b), therefore being icy. The results for smaller hot moons are also of interest, as Rovira-Navarro et al. (2021) have shown that plausible scenarios may arise in which such temperatures are maintained for timescales $\gtrsim$ 1 Gyr.

We will discuss these results in several contexts: in Sec. 3.4.1, we compare our framework against that in previous literature, and we discuss several caveats to our new formulation in Sec. 3.4.2. One may also wonder if perhaps current-generation infrared telescopes may be able to detect objects in this manner, too: we discuss what this would take in Sec. 3.4.3, and follow this up with a discussion on the applicability of spectroastrometry to moon-planet systems other than the ones we have studied in this paper in Sec. 3.4.4. Finally, we make a comparison of spectroastrometry against other methods in Sec. 3.4.5 and discuss what combinations with other methods may possibly allow unambiguous detection, characterisation and confirmation of moon candidates in Sec. 3.4.6.

3.4.1 Comparison to previous work

While we have expanded the framework provided by Agol et al. (2015) to work for closed Keplerian orbits in general (Sec. 3.2.2) and to include additional noise bounds (Sec. 3.2.3), a great deal of conclusions in their work still hold. In particular, the scaling of the signal-to-noise ratio as $S/N \propto (\epsilon T)^{1/2} d^{-2}$ remains generally applicable, and under the assumptions that the detector pixel size is designed to sample the PSF well (i.e. $\alpha \propto \sigma_{PSF}$), that the pointing stability noise is negligible and that the telescope is diffraction-limited we also recover the telescope-diameter proportionality $S/N \propto D^2$. Additionally, while Agol et al. (2015) do not appear to explicitly have taken note of this, (1) in their formulation the noise is a function of the spectral properties of the moon, but not of its orbit (excepting transits), (2) the spectroastrometric signal-to-noise ratio of a single observation can be straightforwardly calculated for a given observation without requiring any a priori knowledge on the nature of the observed system and (3) there exists an optimal time allocation that minimises the noise of an observation that can be well-approximated by quantities that can be known or estimated a priori (Sec. 3.2.4). Each of these conclusions still hold in our expanded formulation.

There are several additions we have gained over this previous work, however. We have shown that the viability of spectroastrometry is relatively insensitive to the orbital parameters of an exomoon with the exception of its semi-major axis and particularly high eccentricities (well exceeding those found in the Solar System). We found an expression for the best-case and worst-case inclinations as well as the expected spectroastrometric signal for a flat prior on moon inclinations. Additionally, one can show from Eq. 3.8 that in the limit of large T/P, $\hat{\boldsymbol{\xi}} \to -[3e/2,\ 0]^T$, such that circular or small-eccentricity orbits become invisible. Further analysis of Eq. 3.8 shows that this already occurs for $T/P \gtrsim 1$. Hence, we should not expect to be able to observe moons with periods on the order of or shorter than our observation time in the relevant filter, both because their semi-major axis and the resulting orbital motion is small, which was already apparent from the work by Agol et al. (2015), but also because their signal is washed out by this time-averaging effect for $T/P \gtrsim 1$. Conversely, highly eccentric moons on short-period orbits may instead become visible precisely *because* of this time-averaging effect. While for ground-based telescopes observation times are unlikely to exceed orbital periods, this is a plausible scenario for space-based observations, which would require far longer observation time to reach a performance similar to large-diameter ground telescopes.

Additionally, we have shown that while background and instrument noise in centroid measurements for a significant ($> 5\sigma$) detection of the planet is likely to be of similar magnitude to the photon noise, the noise due to a pixelated detector (for a well-sampled PSF) and pointing stability of the telescope in question are unlikely to provide major contributions to the centroid noise, and therefore to the spectroastrometric noise.

3.4.2 Limitations on this formulation

A major limitation of the method as developed in this manner is the lack of an expression for speckle noise, which ostensibly does not satisfy the assumption of independence between pixels required for Eq. 3.11. Until this effect can be quantified, these results

should be taken only as representative for moons of far-out or free-floating planets, where speckle noise is negligible, though fortunately the majority of large exomoons are expected to occur around wide-orbit planets (Dobos et al., 2021; Heller &Pudritz, 2015a), beyond the snowline (Inderbitzi et al., 2020). If an expression or estimate for speckle noise in spectroastrometry can be found, we might be able to push spectroastrometry to find moons of close-in planets in reflected light, too, such as the case of an Earth-Moon analogue studied by Agol et al. (2015), though this would require a different (augmented) model of the moons' spectral energy distribution incorporating reflected light.

A second limitation for close-in planets is the lack of inclusion of the planet-moon barycentre movement over the observations in our formulation. While the movement thereof between observations can be accounted for if the orbital properties of the planet about its host are known, the movement throughout the observation will likely have an effect that is worth quantifying in future studies: using the orbital parameters given by Feng et al. (2023), the worst-case angular velocity (i.e. for a face-on orbit at pericentre) for ε Indi Ab is on the order of 0.1 mas/hr, which is of the same order as spectroastrometric effects. For wide-separation planets or edge-on planets observed at their most distant apparent separation, this effect is negligible, however. As our neglect of speckle noise means that wide-separation planets should be preferred to start with, for this effect to become strong will most likely require that speckle noise be dealt with, first.

Another matter that needs mentioning is the fact that there are objects that cannot immediately be distinguished from moons; background objects may, per chance, induce a spectroastrometric signal. Follow-up observations will, however, reject such candidates without issue, given the rapid motion expected of moons about their host that such background objects will not display. Additionally, thermal emission from asymmetric ring systems around planets will cause a signal that may mimic thermal emission from a hot moon; one could foresee such asymmetric rings arising in a miniature version of the scenario invoked by András &Rieke (2020) for the debris cloud formerly identified with Formalhaut b, for example, though notably Formalhaut b was not detectable in the infrared. As such asymmetries on a Keplerian orbit should be expected to dissipate over the order of several orbits, a signal due to such occurrences should not be expected to remain stable over observational timescales; additionally, the presence of rings (asymmetric or not) may be excluded altogether by the method proposed by Lazzoni et al. (2020), for example.

Spots or asymmetric patterns on the planet may produce an astrometric signal, too: we note that the Great Red Spot on Jupiter is dim in the infrared (Ge et al., 2019), and so we should by analogy expect any such effects to stem from larger-scale variability. For Jupiter, such rotational variability is on the order of 1% in flux around the 10.5 μm region, whereas in the 5 μm region this is roughly 20% (Ge et al., 2019). For the moon filter we can thus safely disregard this variability: the planet filter does warrant a small calculation. In the worst-case scenario of a pole-on planet with all this variability concentrated on a single spot at the equator, and with a Jupiter-like radius and rotation period of 10 hours, the resultant astrometric signal will be on the order of 10^{-2} mas. As the 20% variability on Jupiter is the result of large-scale variability, not spot-like localised variability (Ge et al., 2019), we expect that this effect will be significantly smaller in practice. Additionally, higher-mass planets are expected to have a lower rotational period (Snellen et al., 2014),

which will dampen the signal strongly if the rotational period becomes of the same order as the observation time in a filter. Nonetheless, these variability effects may thus, in the worst case, be present at an order of magnitude that will contaminate the most sensitive of our results: follow-up observations in different planet-bands (perhaps with lower variability) will then provide a conclusive result on the presence or absence of a moon.

It is thus possible to exclude background objects, (asymmetric) ring systems, or planet variability either immediately or after follow-up observations. Consequently, we expect that moons are the only objects or phenomena that can be responsible for long-term spectroastrometric signals, though any putative signal will need follow-up observations for confirmation.

3.4.3 Spectroastrometric capabilities of current-generation telescopes

As these results show that observing tidally heated exomoons on future IR telescopes is plausible, one might wonder whether current-generation IR telescopes have the capabilities required to observe tidally heated moons in nearby systems. The prime candidate here, of course, is JWST; unfortunately, the scaling of the signal-to-noise ratio with D^2 suggests that the observation time required would be on the order of days. JWST would thus only be sensitive to hot moons around nearby directly imageable planets that are less luminous than ε Indi Ab, none of which are currently known.

Additionally, while the fine-guidance pointing stability of JWST is of an order similar to that of ELT, target reacquisition (which would be required when switching between filters) only has accuracies on the order of mas (Hartig &Lallo, 2022), which introduces systematic error. This may be remedied if one uses astrometric observations (i.e. using a single filter) of the moon throughout its orbit instead, but in that case it still remains to be shown that the measured effect is due to motion of a moon rather than due to a third object disturbing the Keplerian motion of the planet. In fortituous circumstances, one might also be able to use sufficiently bright background objects (that can be astrometrically positioned to the required accuracy) to reference the observations in the two filters against each other, but this requires that such objects be available and fixed. We leave it to future work to determine the viability of each of these methods to perform spectroastrometric measurements using JWST.

3.4.4 Detectability of other moon-planet systems

In this analysis, we have considered Solar System-like moons around a planet analogous to ε Indi Ab, as it is the nearest known Jupiter analogue that is directly imageable. However, such a system need not be optimal in terms of detectability of any moons; moreover, it is likely that with JWST operational many more directly imageable planets will be discovered in nearby system that had previously eluded detection. It is thus productive to consider what other planets might be found, or perhaps what types of moons might be detectable around them.

One such category is lower-mass planets; exploratory results using the code in this paper suggest that even lower-temperature moons will be observable around lower-mass

planets, as the relative flux of the moon then increases appreciable in the moon filter. If located in a suitable nearby system (such that stellar contamination is not a problem), this may thus allow the detection of true Solar System-analogues: that is to say, Solar System-analogue planets accompanied by Solar System-size and Solar System-temperature moons. Down to Saturn-masses this is hardly problematic, but for lower-mass planets (transitioning into the ice giant-regime) the spectral feature at 5 μm starts to become muted (Roman, 2023; Linder et al., 2019), such that the planet will no longer outshine its moon in that band; another planet filter than M' (which was selected in a fairly ad hoc fashion) is required for ice giants. Detection of moons around such planets would thus require a more robust filter selection procedure than we have followed in our analysis of ε Indi Ab. Hence, we propose that in anticipation of the detection of directly imageable low-mass giant planets in nearby systems by JWST further research is done on filter performance over a wide variety of planet masses and ages.

A second category of systems does not concern the type of planet, but rather the type of moon; while we have for the purposes of our analysis explicitly remained in the familiar realm of Solar System-like moons, current exomoon candidates are ostensibly unlike the moons seen in our Solar System. The candidates put forward by Teachey et al. (2018), Teachey &Kipping (2018), Lazzoni et al. (2020) and Kipping et al. (2022) are perhaps rather thought of as binary objects; this poses unique challenges for spectroastrometry in that the spectra of two gas giant planets in a mutual orbit are likely to posses similar features qualitatively over a broad range of wavelengths. As both objects are, without requiring tidal heating, likely to be relatively bright, however, their spectroastrometric signal may still be detectable, and if so, perhaps at system distances further away than Solar System-like moons. Given the importance of such objects in informing moon formation theory (e.g. Hamers &Portegies Zwart 2018; Hansen 2019; Moraes &Neto 2020), it is worth exploring whether any filter combination might be able to detect or rule out the presence of any such moons; perhaps, even, whether a filter combination may be able to detect both Solar System-like moons and binary-like objects.

3.4.5 Comparing against other moon detection methods

Over other methods, spectroastrometry provides an additional boon in the fact that, if the barycentre motion discussed in Sec. 3.4.2 is accounted for, the astrometry produced is of a sufficient level to potentially detect the orbital motion of nearby exoplanets over a single observation; even in the absence of a moon detection, the data is therefore still useful in novel ways. Another major advantage that spectroastrometry has over the current suite of standard exomoon detection efforts is the lack of degeneracies (if observed over multiple epochs), such as those induced by unseen second planets in the case of the methods proposed for transiting planets (Fox &Wiegert, 2021; Kipping &Teachey, 2020); as one measures explicitly the movement of the moon about its planet, these third-object effects are unambiguously removed. Finally, spectroastrometry provides the possibility of repeatable observations of nearby moons as small and nearly as cold as those observed in the Solar System, far below temperatures required for other direct imaging methods for tidally heated moons (e.g. Kleisioti et al. 2023), while being relatively insensitive to the inclination or orientation of the moon or its planet.

3.4.6 Synergies with other methods

Further modelling of the moon or its orbit can further enhance the significance of results and produce predictions or constraints on quantities such as the semi-major axis, period, size, host planet mass and flux distribution between satellite and host (Agol et al., 2015) and consequently even interior properties of the satellite (e.g. Kleisioti et al. 2023) that can be (independently) verified with other methods, such as radial velocity or astrometric measurements of the planet or such as TTVs/TDVs, auxiliary stellar transits or moon-transits of the planet, if the system is fortituously oriented. Especially noteworthy is the fact that at satellite inclinations where spectroastrometry fares poorest (near edge-on), transits of their host and radial velocity measurements become viable, which makes spectroastrometry a useful complement to those methods. Finally, mutual events (Cabrera &Schneider, 2007) observed in the infrared might provide information on the composition of the planet and moon as well as provide independent constraints on the moon orbit (Schneider et al., 2015).

Another detail of particular interest is the fact that spectroastrometry provides an independent constraint on moon and planet fluxes as well as the moon orbit that may be combined with those derivable from moon-planet models such as discussed in Kleisioti et al. (2023), which can be produced from the same direct imaging data that spectroastrometry can be performed on. In combination with the results derivable from other methods, it is therefore possible to come to a near-full characterisation of the moon in question in terms of its orbit, composition, size and surface conditions.

We would therefore like to emphasise the possible capabilities of simultaneous use of spectroastrometry over multiple epochs, photometric modelling, astrometry and transit observations of moon-transits of the planet, as all of these should in principle be possible with the same series of direct-imaging observations. Given the set of mutually independent estimates for similar parameters available between the set of these, self-consistency of any candidate can be straightforwardly checked. We therefore strongly recommend that the viability of this combination is evaluated in future studies.

3.5 Conclusion

Spectroastrometry has previously been shown to be a promising method for detection of Earth-Moon-like systems or Earth-like moons orbiting Jovians by Agol et al. (2015). We have shown that there is a further class of satellites, tidally heated moons analogous to those in the Solar System, that are observable in nearby systems using this method with next-generation ground telescopes. Illustrated by two example systems motivated by moons observed in our current-day Solar System, we see that for nearby systems even large icy bodies or hot bodies comparable in size to those seen in our Solar System may be observable.

In showing this, we have derived an expression for the spectroastrometric signal that covers all closed Keplerian orbits, along with the orbital motion of the moon throughout the observation, which shows that the efficacy of spectroastrometry is only weakly dependent on the orbital properties of an exomoon, except for moons with periods equal to or lower than the observation time, which are unlikely to be detected. Moreover, we

have derived additional conservative noise estimates for noise due to (1) background and instrument noise, (2) a pixelated detector and (3) pointing inaccuracies. This now allows evaluation of spectroastrometry as a method on telescopes other than the ideal photon-noise limited space telescopes assumed in previous research and without requiring a priori any assumptions on the orbit or nature of any potential moon.

Bibliography

Agol, E., Jansen, T., Lacy, B., Robinson, T. D., & Meadows, V. 2015, The Astrophysical Journal, 812, 5, doi: 10.1088/0004-637X/812/1/5

András, G., & Rieke, G. H. 2020, Proceedings of the National Academy of Sciences, 117, 9712, doi: 10.1073/pnas.1912506117/-/DCSupplemental.y

Bagheri, A., Khan, A., Deschamps, F., et al. 2022, Icarus, 376, doi: 10.1016/j.icarus.2021.114871

Bailey, J. 1998a, Monthly Notices of the Royal Astronomical Society, 301, 161, doi: 10.1046/j.1365-8711.1998.02010.x

Bailey, J. A. 1998b, in Optical Astronomical Instrumentation, Vol. 3355 (SPIE), 932–939, doi: 10.1117/12.316802

Baland, R. M., Van Hoolst, T., Yseboodt, M., & Karatekin, Ö. 2011, Astronomy and Astrophysics, 530, doi: 10.1051/0004-6361/201116578

Batygin, K., & Morbidelli, A. 2020, The Astrophysical Journal, 894, 143, doi: 10.3847/1538-4357/ab8937

Beuthe, M. 2015, Icarus, 258, 239, doi: 10.1016/j.icarus.2015.06.008

—. 2016, Icarus, 280, 278, doi: 10.1016/j.icarus.2016.08.009

Bierson, C. J., & Nimmo, F. 2022, Icarus, 373, doi: 10.1016/j.icarus.2021.114776

Bills, B. G., & Nimmo, F. 2011, Icarus, 214, 351, doi: 10.1016/j.icarus.2011.04.028

Brandl, B., Bettonvil, F., Van Boekel, R., et al. 2021, The Messenger, 182, 22, doi: http://doi.org/10.18727/0722-6691/5218

Burnett, E., & Hayne, P. 2023. http://arxiv.org/abs/2302.13226

Cabrera, J., & Schneider, J. 2007, Astronomy and Astrophysics, 464, 1133, doi: 10.1051/0004-6361:20066111

Canup, R. M., & Ward, W. R. 2006, Nature, 441, doi: 10.1038/nature04860

Carlomagno, B., Delacroix, C., Absil, O., et al. 2020, Journal of Astronomical Telescopes, Instruments, and Systems, 6, doi: 10.1117/1.jatis.6.3.035005

Cilibrasi, M., Szulágyi, J., Mayer, L., et al. 2018, Monthly Notices of the Royal Astronomical Society, 480, 4355, doi: 10.1093/mnras/sty2163

Dobos, V., Charnoz, S., Pál, A., Roque-Bernard, A., & Szabó, G. M. 2021, Publications of the Astronomical Society of the Pacific, 133, doi: 10.1088/1538-3873/abfe04

Dobos, V., Haris, A., Kamp, I. E. E., & van der Tak, F. F. S. 2022, Monthly Notices of the Royal Astronomical Society, 513, 5290, doi: 10.1093/mnras/stac1180

Dobos, V., & Turner, E. L. 2015, Astrophysical Journal, 804, doi: 10.1088/0004-637X/804/1/41

Feng, F., Anglada-Escudé, G., Tuomi, M., et al. 2019, Monthly Notices of the Royal Astronomical Society, 490, 5002, doi: 10.1093/mnras/stz2912

Feng, F., Butler, R. P., Vogt, S. S., Holden, B., & Rui, Y. 2023, Monthly Notices of the Royal Astronomical Society, 525, 607, doi: 10.1093/mnras/stad2297

Forgan, D., & Dobos, V. 2016, MNRAS, 457, 1233, doi: 10.1093/mnras/stw024

Fox, C., & Wiegert, P. 2021, Monthly Notices of the Royal Astronomical Society, 501, 2378, doi: 10.1093/mnras/staa3743

Fuller, J., Luan, J., & Quataert, E. 2016, Monthly Notices of the Royal Astronomical Society, 458, 3867, doi: 10.1093/mnras/stw609

Gaeman, J., Hier-Majumder, S., & Roberts, J. H. 2012, Icarus, 220, 339, doi: 10.1016/j.icarus.2012.05.006

Ge, H., Zhang, X., Fletcher, L. N., et al. 2019, The Astronomical Journal, 157, 89, doi: 10.3847/1538-3881/aafba7

Hamers, A. S., & Portegies Zwart, S. F. 2018, The Astrophysical Journal, 869, L27, doi: 10.3847/2041-8213/aaf3a7

Han, C. 2008, The Astrophysical Journal, 684, 684

Han, C., & Han, W. 2002, The Astrophysical Journal, 580, 490. http://exoplanets.org.

Hansen, B. M. S. 2019, Science Advances, 5. https://www.science.org

Hartig, G., & Lallo, M. 2022, JWST Line-of-Sight Jitter Measurement during Commissioning, Tech. rep., STScI. https://soccer.stsci.edu

Heller, R., & Pudritz, R. 2015a, Astronomy and Astrophysics, 578, doi: 10.1051/0004-6361/201425487

—. 2015b, Astrophysical Journal, 806, doi: 10.1088/0004-637X/806/2/181

Heller, R., Williams, D., Kipping, D., et al. 2014, Formation, habitability, and detection of extrasolar moons, Mary Ann Liebert Inc., doi: 10.1089/ast.2014.1147

Hippke, M. 2015, Astrophysical Journal, 806, doi: 10.1088/0004-637X/806/1/51

Hu, R., Ehlmann, B. L., & Seager, S. 2012, Astrophysical Journal, 752, doi: 10.1088/0004-637X/752/1/7

Hussmann, H., Sohl, F., & Spohn, T. 2006, Icarus, 185, 258, doi: 10.1016/j.icarus.2006.06.005

Hwang, K.-H., Udalski, A., Bond, I. A., et al. 2018, The Astronomical Journal, 155, 259, doi: 10.3847/1538-3881/aac2cb

Inderbitzi, C., Szulágyi, J., Cilibrasi, M., & Mayer, L. 2020, Monthly Notices of the Royal Astronomical Society, 499, 1023, doi: 10.1093/mnras/staa2796

Jones, A., Noll, S., Kausch, W., Szyszka, C., & Kimeswenger, S. 2013, Astronomy and Astrophysics, 560, doi: 10.1051/0004-6361/201322433

Kaltenegger, L. 2010, The Astrophysical Journal Letters, 712, 125, doi: 10.1088/2041-8205/712/2/L125

Kenworthy, M. A., & Mamajek, E. E. 2015, Astrophysical Journal, 800, doi: 10.1088/0004-637X/800/2/126

Kipping, D. 2020, The Astrophysical Journal, 900, L44, doi: 10.3847/2041-8213/abafa9

Kipping, D., & Teachey, A. 2020, Serbian Astronomical Journal, 25, doi: 10.2298/SAJ2001025K

Kipping, D., & Yahalomi, D. A. 2022, Monthly Notices of the Royal Astronomical Society, 518, 3482, doi: 10.1093/mnras/stac3360

Kipping, D., Bryson, S., Burke, C., et al. 2022, Nature Astronomy, 6, 367, doi: 10.1038/s41550-021-01539-1

Kipping, D. M. 2009a, Monthly Notices of the Royal Astronomical Society, 392, 181, doi: 10.1111/j.1365-2966.2008.13999.x

—. 2009b, Monthly Notices of the Royal Astronomical Society, 396, 1797, doi: 10.1111/j.1365-2966.2009.14869.x

Kleisioti, E., Dirkx, D., Rovira Navarro, M., & Kenworthy, M. 2021, in Proceedings of the Europlanet Science Congress 2021, doi: 10.5194/epsc2021-546

Kleisioti, E., Dirkx, D., Rovira-Navarro, M., & Kenworthy, M. A. 2023, Astronomy & Astrophysics. http://arxiv.org/abs/2305.03410

Lainey, V. 2016, Celestial Mechanics and Dynamical Astronomy, 126, 145, doi: 10.1007/s10569-016-9695-y

Lainey, V., Casajus, L. G., Fuller, J., et al. 2020, Nature Astronomy, 4, 1053, doi: 10.1038/s41550-020-1120-5

Lammer, H., Schiefer, S. C., Juvan, I., et al. 2014, Origins of Life and Evolution of Biospheres, 44, 239, doi: 10.1007/s11084-014-9377-2

Lazzoni, C., Desidera, S., Gratton, R., et al. 2022, Monthly Notices of the Royal Astronomical Society, 516, 391, doi: 10.1093/mnras/stac2081

Lazzoni, C., Zurlo, A., Desidera, S., et al. 2020, Astronomy and Astrophysics, 641, doi: 10.1051/0004-6361/201937290
Li, D., Johansen, A., Mustill, A. J., Davies, M. B., & Christou, A. A. 2020, Astronomy and Astrophysics, 638, doi: 10.1051/0004-6361/201936672
Limbach, M. A., & Turner, E. L. 2013, Astrophysical Journal, 769, doi: 10.1088/0004-637X/769/2/98
Limbach, M. A., Vos, J. M., Winn, J. N., et al. 2021, The Astrophysical Journal Letters, 918, L25, doi: 10.3847/2041-8213/ac1e2d
Linder, E. F., Mordasini, C., Mollière, P., et al. 2019, Astronomy and Astrophysics, 623, doi: 10.1051/0004-6361/201833873
Lombardi, G., Zitelli, V., & Ortolani, S. 2009, Monthly Notices of the Royal Astronomical Society, 399, 783, doi: 10.1111/j.1365-2966.2009.15309.x
Lunine, J. I., & Nolan, M. C. 1992, Icarus, 100, 221
Markley, F. L. 1995, Celestial Mechanics and Dynamical Astronomy, 63, 101
McKinnon, W. B., & Benner, L. A. M. 1990, in Abstracts of the Lunar and Planetary Science Conference, Vol. 21, 777–778
McKinnon, W. B., & Kirk, R. L. 2014, in Encyclopedia of the Solar System (Elsevier), 861–881, doi: 10.1016/b978-0-12-415845-0.00040-2
Moraes, R., & Neto, E. V. 2020, Monthly Notices of the Royal Astronomical Society, 495, 3763, doi: 10.1093/mnras/staa1441
Moraes, R. A., Kley, W., & Vieira Neto, E. 2018, Monthly Notices of the Royal Astronomical Society, 475, 1347, doi: 10.1093/mnras/stx3268
Nakajima, M., Genda, H., Asphaug, E., & Ida, S. 2022, Nature Communications, 13, doi: 10.1038/s41467-022-28063-8
Nimmo, F., & Pappalardo, R. T. 2016, Journal of Geophysical Research: Planets, 121, 1378, doi: 10.1002/2016JE005081
Nimmo, F., & Spencer, J. R. 2015, Icarus, 246, 2, doi: 10.1016/j.icarus.2014.01.044
Nimmo, F., Hamilton, D. P., McKinnon, W. B., et al. 2016, Nature, 540, 94, doi: 10.1038/nature20148
Noll, S., Kausch, W., Barden, M., et al. 2012, Astronomy and Astrophysics, 543, doi: 10.1051/0004-6361/201219040
Oberg, N., Cazaux, S., Kamp, I., et al. 2023, Astronomy & Astrophysics, 672, A142. http://arxiv.org/abs/2302.14425
Oza, A. V., Johnson, R. E., Lellouch, E., et al. 2019, The Astrophysical Journal, 885, 168, doi: 10.3847/1538-4357/ab40cc
Phillips, M. W., Tremblin, P., Baraffe, I., et al. 2020, Astronomy and Astrophysics, 637, doi: 10.1051/0004-6361/201937381
Porter, J. M., Oudmaijer, R. D., & Baines, D. 2004, Astronomy and Astrophysics, 428, 327, doi: 10.1051/0004-6361:20035686
Prusti, T., De Bruijne, J. H., Brown, A. G., et al. 2016, Astronomy and Astrophysics, 595, doi: 10.1051/0004-6361/201629272
Rodeghiero, G., Arcidiacono, C., Pott, J.-U., et al. 2021, J. Astron. Telesc. Instrum. Syst., 7. https://www.spiedigitallibrary.org/journals/Journal-of-Astronomical-Telescopes,-Instruments,-and-Systems
Roman, M. T. 2023, Remote Sensing, 15, 1811, doi: 10.3390/rs15071811
Ross, M. N., & Schubert, G. 1990, Geophysical Research Letters, 17, 1749, doi: 10.1029/GL017i010p01749
Rovira-Navarro, M., Matsuyama, I., & Hay, H. C. F. C. 2023, The Planetary Science Journal, 4, 23, doi: 10.3847/psj/acae9a

Rovira-Navarro, M., Van Der Wal, W., Steinke, T., & Dirkx, D. 2021, The Planetary Science Journal, 2, 119, doi: 10.3847/PSJ/abf6cb

Ruffio, J.-B., Horstman, K., Mawet, D., et al. 2023, The Astronomical Journal, 165, 113. http://arxiv.org/abs/2301.04206

Saillenfest, M., Sulis, S., Charpentier, P., & Santerne, A. 2023, Astronomy & Astrophysics, 675, A174. http://arxiv.org/abs/2306.07348

Schenk, P. M., Beddingfield, C. B., Bertrand, T., et al. 2021, Remote Sensing, 13, doi: 10.3390/rs13173476

Schneider, J., Lainey, V., & Cabrera, J. 2015, International Journal of Astrobiology, 14, 191, doi: 10.1017/S1473550414000299

Segatz, M., Spohn, T., Ross, M. N., & Schubert, G. 1988, ICARUS, 75, 187

Snellen, I. A., Brandl, B. R., De Kok, R. J., et al. 2014, Nature, 508, 63, doi: 10.1038/nature13253

Squyres, S. W. 1980, ICARUS, 44, 502

Teachey, A., Kipping, D., Burke, C. J., Angus, R., & Howard, A. W. 2020, The Astronomical Journal, 159, 142, doi: 10.3847/1538-3881/ab7001

Teachey, A., & Kipping, D. M. 2018, Science Advances, 4, eaav1784. https://www.science.org

Teachey, A., Kipping, D. M., & Schmitt, A. R. 2018, The Astronomical Journal, 155, 36, doi: 10.3847/1538-3881/aa93f2

Tokadjian, A., & Piro, A. L. 2022, The Astrophysical Journal Letters, 929, L2, doi: 10.3847/2041-8213/ac61e8

Vallenari, A., Brown, A. G. A., Prusti, T., et al. 2023, Astronomy & Astrophysics, 674, A1, doi: 10.1051/0004-6361/202243940

Vanderburg, A., Rappaport, S. A., & Mayo, A. W. 2018, The Astronomical Journal, 156, 184, doi: 10.3847/1538-3881/aae0fc

Whelan, E., & Garcia, P. 2008, Spectro-astrometry: The method, its limitations, and applications, doi: 10.1007/978-3-540-68032-1{_}6

Whittaker, E. A., Malik, M., Ih, J., et al. 2022, The Astronomical Journal, 164, 258, doi: 10.3847/1538-3881/ac9ab3

Williams, D. M., Kasting, J. F., & Wade, R. A. 1997, Nature, 385, 234